ChemSusChem

Research Article
doi.org/10.1002/cssc.202400084

Chemistry Europe
European Chemical Societies Publishing

www.chemsuschem.org

Mo_3S_{13} Chalcogel: A High-Capacity Electrode for Conversion-Based Li-Ion Batteries

Taohedul Islam,[a] Subrata Chandra Roy,[a] Sahar Bayat,[b] Misganaw Adigo Weret,[a] Justin M. Hoffman,[c] Keerthan R. Rao,[b] Conrad Sawicki,[d] Jing Nie,[a] Robiul Alam,[a] Oluwaseun Oketola,[a] Carrie L. Donley,[e] Amar Kumbhar,[e] Renfei Feng,[f] Kamila M. Wiaderek,[c] Chad Risko,[b] Ruhul Amin,*[d] and Saiful M. Islam*[a]

Despite large theoretical energy densities, metal-sulfide electrodes for energy storage systems face several limitations that impact the practical realization. Here, we present the solution-processable, room temperature (RT) synthesis, local structures, and application of a sulfur-rich Mo_3S_{13} chalcogel as a conversion-based electrode for lithium-sulfide batteries (LiSBs). The structure of the amorphous Mo_3S_{13} chalcogel is derived through *operando* Raman spectroscopy, synchrotron X-ray pair distribution function (PDF), X-ray absorption near edge structure (XANES), and extended X-ray absorption fine structure (EXAFS) analysis, along with ab initio molecular dynamics (AIMD) simulations. A key feature of the three-dimensional (3D) network is the connection of Mo_3S_{13} units through S–S bonds. Li/Mo_3S_{13} half-cells deliver initial capacity of 1013 mAh g^{-1} during the first discharge. After the activation cycles, the capacity stabilizes and maintains 312 mAh g^{-1} at a C/3 rate after 140 cycles, demonstrating sustained performance over subsequent cycling. Such high-capacity and stability are attributed to the high density of (poly)sulfide bonds and the stable Mo–S coordination in Mo_3S_{13} chalcogel. These findings showcase the potential of Mo_3S_{13} chalcogels as metal-sulfide electrode materials for LiSBs.

1. Introduction

■■Please provide academic titles (Prof., Dr.) for all authors■■

■■Dear author, please provide a TOC picture. This will appear together with the TOC figure on the first pages of the online issue, if your article will become part of this issue.■■

Lithium-ion battery (LIB) technologies continue to play a prominent and growing role since their initial commercialization by Sony in 1991.[1] Commercial LIBs typically use lithium metal oxides (LMO_2) as the cathode and graphite as the anode, a design that has been in place since Yoshino's invention of intercalation-based charge-discharge process.[2–4] However, the theoretical specific capacities of both cathodes and anodes are not large enough to meet the growing demands of many storage needs. Therefore, the exploration for alternative electrode materials with increased capacity continues to be a scientific and technological focal point.

Conversion-based lithium-sulfide batteries (LiSBs) possess a high theoretical specific capacity of 1672 mAh g^{-1} and a predicted specific energy of ~2600 Wh kg^{-1}, metrics that are significantly higher than graphite-LMO_2 batteries.[5,6] The large energy density is attributed to the stepwise involvement of 16 electrons in the formation of Li_2S from S_8 ($S_8 + Li^+ + 16e^- \rightarrow 8Li_2S$), compared to the participation of one- electron in the formation of LiC_6 in graphite-LMO_2 batteries.[7] Despite these intriguing characteristics, LiSBs have their own issues, such as the low conductivity of S, large volume change during the charge-discharge process, lithium corrosion, the growth of Li dendrites, and dissolution of polysulfide (Li_2S_x) leading to the loss of active materials.[7–11]

To counter the issues associated with conversion-based LIBs, transition metal sulfides as "sulfur-equivalent" electrodes have been investigated.[12–14] Since the covalent bonds between transition metals and sulfur are stronger than the ionic interactions of lithium and sulfur, transition metal sulfide electrodes can contribute to reducing sulfur dissolution into the electrolyte. Moreover, these materials offer a high gravimetric capacity similar to sulfur-based electrodes, given that the conversion of sulfur into lithium sulfide is the plausible mechanism in LiSBs.[12,15–17] Several transition metal sulfides have been employed as conversion-based LiSBs electrode materials, including: α-MnS,[18] FeS,[19] Co_9S_8,[20] NiS,[21] and Ni_3S_2,[22] transi-

[a] *T. Islam, S. Chandra Roy, M. Adigo Weret, J. Nie, R. Alam, O. Oketola, S. M. Islam*
Department of Chemistry, Physics, and Atmospheric Sciences, Jackson State University, 39217 Jackson, MS, USA
E-mail: muhammad.s.islam@jsums.edu

[b] *S. Bayat, K. R. Rao, C. Risko*
Department of Chemistry & Center for Applied Energy Research, University of Kentucky, 40506-0055 Lexington, KY, USA

[c] *J. M. Hoffman, K. M. Wiaderek*
X-ray Science Division, Advanced Photon Source, Argonne National Laboratory, 60439 Argonne, Illinois, USA

[d] *C. Sawicki, R. Amin*
Electrification and Energy Infrastructures Division, Oak Ridge National Laboratory, Hardin Valley Campus, 37830 Knoxville, TN, USA
E-mail: aminr@ornl.gov

[e] *C. L. Donley, A. Kumbhar*
Department of Chemistry, University of North Carolina at Chapel Hill, 27599-3290 Chapel Hill, NC, USA

[f] *R. Feng*
Canadian Light Source, S7 N2 V3 Saskatoon, Saskatchewan, Canada

Supporting information for this article is available on the WWW under https://doi.org/10.1002/cssc.202400084

tion metal disulfides, FeS_2,[23] CoS_2,[24] Mo-doped NiS_2,[25] MoS_2,[26] WS_2,[27] ZrS_2,[28] and VS_2;[29] and transition metal trisulfides, amorphous MoS_3,[30] and WS_3.[31] However, the lack of cyclic stability of these metal sulfides during the charge-discharge process limits their application in LiSBs.[19,24,32] Moreover, crystalline metal sulfides undergo a large volume change during lithiation and de-lithiation, which presents difficulty for practical application in LiSBs.[33–35] Hence, there is a need to continue exploring for novel materials to overcome the issues, including cyclic instability, volume change and other.

Chalcogenide-based aerogels, known as chalcogels, are a unique class of low-density micro- to macro-porous materials that possess a structural backbone composed of a polysulfide network, enabling them to mimic sulfur-equivalent electrodes for LiSBs.[36,37] Hence, the inherent properties of chalcogels, such as porosity, semiconductivity, amorphous structure, and the presence of metal-sulfur covalent bonds in their ultra-small nanoparticles, confer significant advantages over pure sulfur electrodes.[38,39] Specifically, chalcogels with these properties can facilitate ion transport, enhance electrical conductivity, minimize sulfide dissolution in the electrolyte, promote facile structural rearrangement during charge-discharge cycles, and thus collectively contribute to the chemical and cyclic stability of sulfur-based electrodes. Our prior work demonstrated MoS_x chalcogel (synthesized using the MoS_4^{2-} precursor) as sulfur-equivalent cathode for LiSBs,[36] showing the potential of these materials to be utilized as high-capacity electrodes in metal sulfide batteries.

Here, we report the solution-processable, room-temperature (RT), and scalable synthesis of an amorphous Mo_3S_{13} chalcogel. Using synchrotron X-ray PDF, XANES, EXAFS, and AIMD simulations, we show that the local structure of the Mo_3S_{13} chalcogel is akin to the precursor $Mo_3S_{13}^{2-}$ cluster, demonstrating that its bulk structure is formed through the coordination among the precursor anions. The electrochemical charge-discharge characteristics of Li/Mo_3S_{13} cells reveal a specific capacity of 312 mAh g^{-1} after 140 cycles at a C/3 rate, showcasing the stability of the cell with no indication of a notable capacity loss in the successive cycles. The combination of RT and scalable synthesis of Mo_3S_{13} chalcogel, along with its high capacity and cycle efficiency, positions it as a promising metal-sulfide electrode material for LiSBs.

2. Results and Discussion

2.1. Synthesis and Gelation Mechanisms

The Mo_3S_{13} chalcogel was synthesized in solution at ambient conditions. Specifically, from a mixture of the solutions of $(NH_4)_2Mo_3S_{13}$ and I_2 in Formamide, the monolith Mo_3S_{13} chalcogel was obtained in 24 hours, and aged for 48 hours. During the gelation of the Mo_3S_{13} gel, I^- anions counter-balanced the NH_4^+ cation, as shown in Equation (1). Details about the synthesis conditions are reported in the Experimental Methods.

$$(NH_4)_2Mo_3S_{13(sol)} + I_{2(sol)} \rightarrow Mo_3S_{13(gel)} + 2NH_4^+{}_{(sol)} + 2I^-{}_{(sol)} \quad (1)$$

It is important to note that immediately after precursor addition, the solution becomes viscous, suggesting the initiation of rapid chemical interactions. Along with this observation, *operando* Raman spectroscopy shows broad bands after 10 minutes of gelation in the regions of 550–530 cm^{-1} and 396–296 cm^{-1}. However, these bands were absent in the solutions of individual species of $(NH_4)_2Mo_3S_{13}$ and I_2 (Figure 1A). The bands at 550 and 530 cm^{-1} are related to the vibrational stretching of the Mo_3S_{13} cluster for bridging and terminal disulfides, ν(S–S),

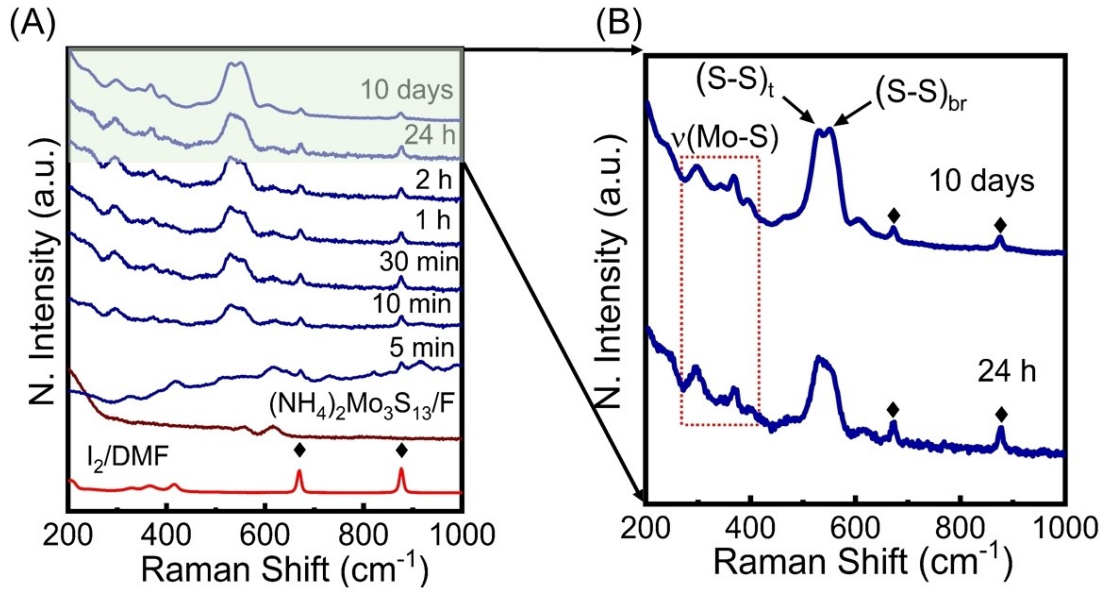

Figure 1. *Operando* Raman spectra during the gelation of Mo_3S_{13} chalcogel (A), Raman spectra of Mo_3S_{13} chalcogel after 24 h and 10 days (B), (red box indicates the Mo–S vibrational bonds, black tetragons represent peaks from iodine solution).

respectively.[40,41] The bands in the range of 396–296 cm^{-1} originate from the ν(Mo–S) vibrations.[41,42] These findings suggest the formation of a random network of the chalcogel having Mo–S clusters similar to the $Mo_3S_{13}^{2-}$ anion of the precursor $(NH_4)_2Mo_3S_{13}$.

After synthesizing the solution-containing gels (called "wet gel"), (Figure 2A), the aerogel was fabricated by drying the wet gel following the supercritical drying method using liquid CO_2 at supercritical conditions (see Experimental Methods). The xerogel of Mo_3S_{13} chalcogel was prepared by drying the wet gel at RT and ambient pressure. Solid-state UV/Vis spectra of the Mo_3S_{13} wet gels and xerogels reveal a bandgap energy of 1.75 and 1.40 eV, respectively. This suggests that Mo_3S_{13} is a medium bandgap semiconductor (Figure S1). Hence the difference in the bandgaps in the colloidal sized particles of Mo_3S_{13} wet gels/aerogels and relatively larger particles of xerogels is attributed to quantum confinement effects – phenomenon that already been well documented for chalcogels.[42–44]

2.2. Morphology Analysis

Scanning electron microscopy (SEM) reveals the presence of porous aggregated nanoparticles extending in three dimensions (Figure 2B). Energy dispersive X-ray spectroscopy (EDS) shows the presence of Mo and S in the chalcogel (Figure S2) with the molybdenum-to-sulfur ratio of 1 : 4.31 (Table S1) which infers to the formula Mo_3S_{13}. The morphology and the physical structure of the Mo_3S_{13} aerogel were also investigated by imaging with transmission electron microscopy (TEM), high-angle annular dark-field (HAADF), and scanning tunneling electron microscopy (STEM) with z-contrast (Figure 2C–D) which show the presence of large density of porosity with variable sizes, ranging from meso- to macro-porosity (Figure 2B–D). High-resolution TEM (HRTEM) does not show the presence of any lattice fringes across the gel matrix, suggesting the absence of crystalline entity (Figure 2E). Selected area electron diffraction (SAED) reveals diffuse rings, further confirming the amorphous nature of the Mo_3S_{13} gel particles (Figure 2F).

The evidence of the high-density of porosity of the Mo_3S_{13} chalcogel was further evaluated by the surface area measurements (Figure 2G), which revealed the Brunauer–Emmett–Teller (BET) surface area of 116.45 m^2/g. BET measures the multi-point specific surface area of an analyte under continuous N_2 flow. The surface area measurement revealed a Type-II isotherm consisting of an H1 hysteresis loop (Figure 2G), which indicates the presence of both meso- and macro-porosity in the chalcogel matrix,[37,45] and from the dV/dD plot (Figure S3) we

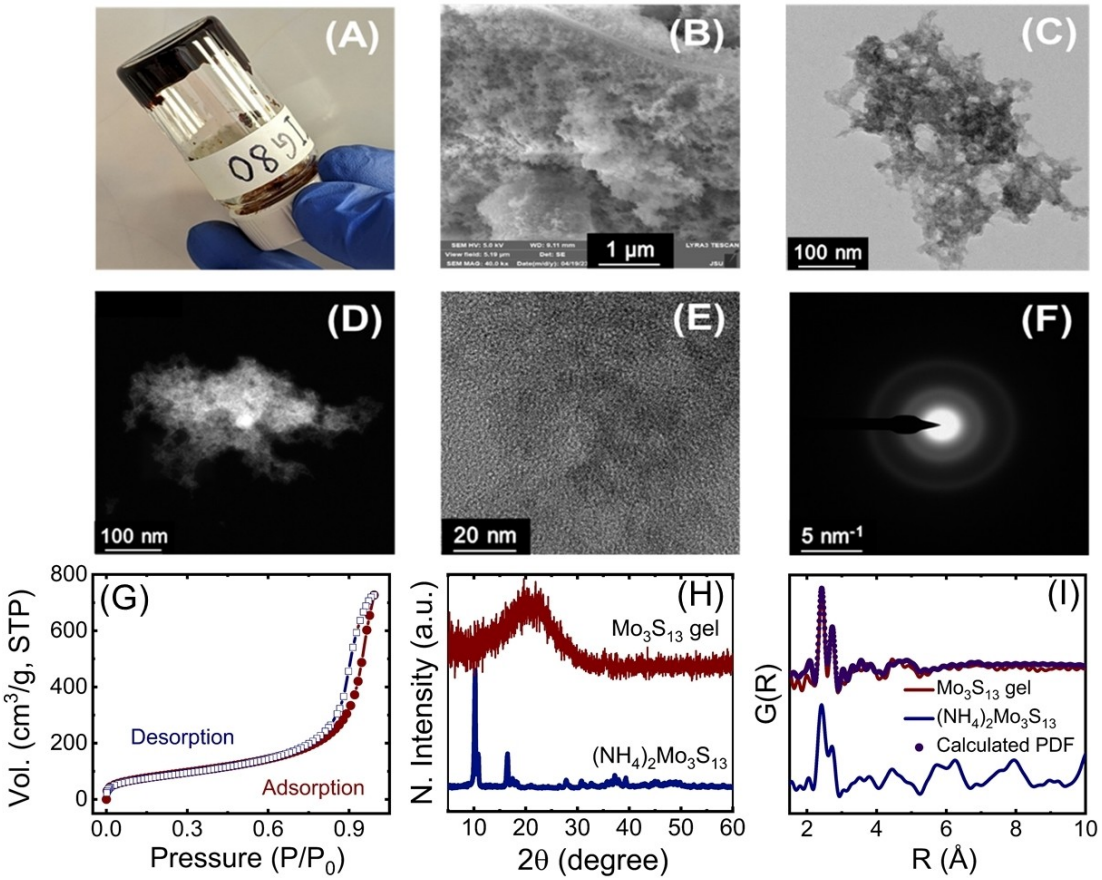

Figure 2. Photograph of the wet gel of Mo_3S_{13} (A), SEM (B), TEM (C), HAADF-STEM (D), HRTEM (E) and SAED (F) showing the morphology, porosities, and the amorphous feature of the gel particles. N_2 adsorption/desorption isotherm for Mo_3S_{13} aerogel showing Type II isotherm with H1 hysteresis (G), powder XRD of Mo_3S_{13} gel (red) presents a featureless diffractogram suggesting an amorphous structure (H), and PDF of the Mo_3S_{13} chalcogel showing lack of long-range order that is consistent with the calculated PDF using isolated $Mo_3S_{13}^{2-}$ cluster (I).

can denote that the size of the pores present on the gel surface mostly ranges from 2–6 nm which further justifies the previous claim of the pore structure of Mo_3S_{13} chalcogel. X-ray powder diffraction of the Mo_3S_{13} chalcogels is featureless, except for a broad hump around 2θ of 23° (Figure 2H). These XRD features are indicative of the absence of periodically ordered atomic arrangement. This finding agrees with the results obtained by HRTEM and SAED, as discussed above.

2.3. Local Structure Determination

To investigate the local structure of the amorphous Mo_3S_{13} chalcogel, we conducted synchrotron total X-ray scattering (TXS) with PDF analysis at Sector 11-ID-B of the Advanced Photon Source (APS) with X-ray energy of 86.7 keV. PDF pattern gives a histogram of the atomic distances, known as pair-correlations, within the material of interest, without the need for Bragg peaks. It can also be simulated based on candidate short-range structures to gain understanding of the basic building blocks within amorphous materials. The PDF of the Mo_3S_{13} gels shows the absence of long-range atomic correlations, but the presence of short-range ordering (Figure 2I). The PDF pattern of the Mo_3S_{13} chalcogel has an intense peak at 2.42 Å representing the Mo–S bonding; this correlation is related to the average Mo–S interatomic distance in the crystal structure of $(NH_4)_2Mo_3S_{13}$.[46,47] The bonding correlation at 2.03 Å represents the S–S bond present in the solid-state matrix of the Mo_3S_{13} gel. The peak at about 2.71 Å represents the Mo–Mo bond distance for the trinuclear Mo_3 cluster in the vicinity of sulfides, similar to the precursor molecule of $(NH_4)_2Mo_3S_{13}$ (Figure 2I).[46] The largest atomic distance in the Mo_3S_{13} cluster in the $(NH_4)_2Mo_3S_{13}$ crystal structure is ~6.9 Å, and the experimental data does not show a noticeable peak above 5 Å, suggesting that the Mo_3S_{13} clusters are connected in a random manner and that the clusters themselves are at least somewhat disordered intrinsically. To model the structures, the Diffpy-CMI program was used, which allows for fitting of several structural parameters including isotropic atomic displacement parameters (ADPs) to account for atomic disorder.[48] We set different ADPs for Mo and S atoms to account for differences in the disorder for different atom types. Here, we used the Debye equation to calculate the scattering pattern of a non-periodic model of a single Mo_3S_{13} cluster. Figure S4 shows that a good-quality fit where R_w value of 0.342 is achieved. The main discrepancies between the calculated and experimental data are from the additional peaks in the calculated pattern arising from discrete Mo–S and S–S distances, which are not present in the more disordered experimental structure. However, the fits are overall similar in shape and intensity. In particular, it is noteworthy that APD_S is 0.931, significantly larger than ADP_{Mo} (Figure S4), indicating that the sulfur atoms are more disordered than the rigid Mo_3 core.

AIMD simulations were also used to evaluate the amorphous Mo_3S_{13} structures. Full details of the simulation protocols are described in the Experimental Methods. Analyses of the pair-correlation functions (PCF) of the AIMD-based Mo_3S_{13} structure show that Mo atoms form heteropolar Mo–S bonds with lengths that peak at 2.34 Å, and homopolar Mo–Mo bonds that have a fairly broad distribution that peaks at 2.78 Å. S–S bonds are observed at 2.09 Å. These bond lengths are comparable to the average bond lengths of Mo–S (2.41 Å), Mo–Mo (2.83 Å), and S–S (2.07 Å) determined from the DFT-optimized structure after the AIMD simulation, using ASE software package.[49] Overall, these bond lengths agree well with those derived from the TXS measurements (Figure S5 and Table S2), validating the AIMD and DFT approaches. Importantly, the complete set of experimental data and simulation results provide confidence in the assignment of the Mo_3S_{13} structure.

X-ray photoelectron spectroscopy (XPS) was conducted to identify elements and determine the formal charge for each atom of the Mo_3S_{13} chalcogel. The strong peaks centered at around 229.53 and 232.73 eV with a splitting energy of $\sim\Delta BE = 3.2$ eV correspond to the binding energy for the $3d_{3/2}$ and $3d_{5/2}$ orbitals of Mo (Figure 3A) that matches with the binding energies of Mo^{4+} in the vicinity of sulfides.[37,47,50,51] The peak centered at 227.58 eV is related to the S 2 s orbital (Figure 3A).[52,53] Deconvolution of the S 2p peaks in the range of 161 to 165 eV shows the existence of multiple doublets (Figure 3B). The peak at ~162.11 eV suggests the presence of monosulfide (S^{2-}), while the peak at~163.42 eV represents the disulfide (S_2^{2-}) bonds (Figure 3B).[37,52,53] The broad S 2p band at ~168.65 eV indicates oxidation of the surface sulfur of the chalcogel's nanoparticles (Figure 3B), which is attributed to prolonged exposure of the wet gel to water and air, especially during the washing and drying process. This feature is common in chalcogels/sulfur-containing materials.[37,42,54,55]

Synchrotron X-ray absorption spectroscopy (XAS) was utilized to further understand the local structure of the amorphous Mo_3S_{13} chalcogel. Figure 3C compares the XANES spectra of the crystalline molecular precursor of $(NH_4)_2Mo_3S_{13}$ and its corresponding Mo_3S_{13} chalcogel. The XANES spectrum of the crystalline $(NH_4)_2Mo_3S_{13}$ precursor mostly overlaps with the XANES of Mo_3S_{13} chalcogel, suggesting similarity in the electronic structures and coordination environments of Mo.

The energy threshold for the photoelectron excitation to go beyond the atomic potential or the absorption edge energy (E_o) for Mo K-edge of the Mo_3S_{13} chalcogel and the $(NH_4)_2Mo_3S_{13}$ were observed at around 2007 eV. A slight shift of the adsorption edge in the Mo_3S_{13} gels may be related to a variation in overall oxidation states of Mo and its chemical environment. We further observe a shoulder through the rising edge of the pristine $(NH_4)_2Mo_3S_{13}$, which may be attributed to the shake-down transition;[56] such a transition arises due to the presence of a core hole that lowers the energy of the metal d orbital, which in turn may facilitate ligand-to-metal charge transfer (LMCT).[56] This transition is not distinctive for the Mo K-edge of the Mo_3S_{13} chalcogel. This indistinctive feature could be related to the disordered atomic arrangement in the amorphous structure.

EXAFS analysis of the Mo K-edge data of the Mo_3S_{13} chalcogel was conducted using the crystalline $(NH_4)_2Mo_3S_{13}$ as a reference (Figure 3D).[46,47] The FEFF calculations were done

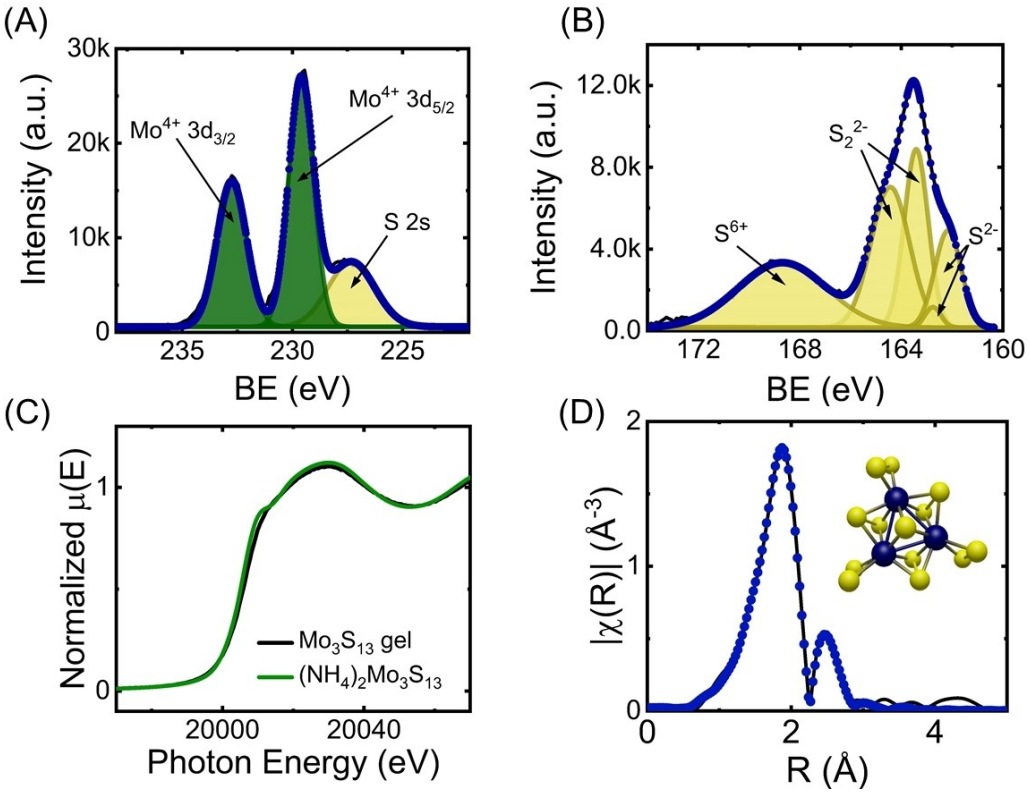

Figure 3. XPS of molybdenum, Mo (A) and sulfur, S (B) showing the oxidation states of the species present on the surface of the nanoparticles of Mo_3S_{13} chalcogel (black line: data, blue dots: fit). Mo K-edge XANES (C), and EXAFS fitting (black line: data, blue dots: fit) of Mo_3S_{13} gel, inset showing the Mo_3S_{13} cluster (D), (blue ball: molybdenum, yellow ball: sulfur).

using FEFF 8 L algorithm[57] and the fitting results are tabulated in Table S3. The EXAFS fitting of the Mo_3S_{13} chalcogel reveals that its local structure resembles to $Mo_3S_{13}^{2-}$ molecular anion. The modeling of the chalcogel's EXAFS data using the crystalline $(NH_4)_2Mo_3S_{13}$ yielded an R factor of ~0.0067, which suggests a quite reasonable fitting of the data. The fitting yielded scattering path lengths of 2.36 Å for Mo–S and 2.69 Å for Mo–Mo. These values closely align with the respective bond lengths in the pristine $(NH_4)_2Mo_3S_{13}$, signifying a strong local structural similarity.[46,51] Most likely, the Mo–S scattering path at 3.87 Å from the fitting represents the photoelectron scattering distance between the absorber Mo of the Mo_3 cluster for the 1st coordination sphere (cluster-1) and a S atom of the 2nd coordination sphere (cluster-2) and indicating the existence of an intercluster ($-S-Mo^{cluster-1}.....^{cluster-2}S-Mo-$) bonding network.[42]

It is important to note that despite similarities in the synthetic process for MoS_x and Mo_3S_{13} gels, their gelation process takes different approaches. Specifically, the reported MoS_x was synthesized using $Mo^{VI}S_4^{2-}$ as precursors, which undergo redox-driven formation of $Mo^{IV}S_x$ gels followed by massive atomic rearrangement and changes in electronic states of Mo ($Mo^{6+}\rightarrow Mo^{4+}$) and S ($S^{2-}\rightarrow S^{-}$).[36] In contrast, based on XPS, XANES, and EXAFS analysis, we determined that the $Mo^{IV}{}_3S_{13}$ chalcogel synthesized from $Mo^{IV}{}_3S_{13}^{2-}$ anions as precursors is formed by the interconnection of the $Mo_3S_{13}^{2-}$ units via S–S bonding. This may occur through the cleavage of the terminal disulfide group $(S_2)^{2-}$ of one $Mo_3S_{13}^{2-}$ anion, followed by the linking of the cleaved terminal $(S_2)^{2-}$ of neighboring $Mo_3S_{13}^{2-}$ anion, without undergoing massive atomic and electronic rearrangement as demonstrated in the MoS_x chalcogels. Hence, this kind of gelation may demonstrate the formation of phase pure and stable product.

2.4. Electrochemical Properties

The electrochemical performance of the Mo_3S_{13} gel was investigated by galvanostatic cycling with potential limitation (GCPL), cyclic voltammetry (CV), electrochemical impedance spectroscopy (EIS), differential capacity plot (dQ/dV plot), and the rate performance (Figure 4A–E). Mo_3S_{13} xerogel was used as electrode in LIBs half-cell configuration. The batteries were cycled from 0.05 V to 3.50 V at a C/3 current rate at RT (Figure S6A). The initial discharge capacity of the Li/Mo_3S_{13} cell was 1013 mAh g^{-1}. The capacity faded quickly for the first few cycles. This feature can be attributed to several issues, including the formation of thick passivation layer on electrode surface, irreversible binding of Li^+ deeper into the voids of the gel matrix, blocking some of the pores of the gel particles, electrolyte decomposition, or an increase of the internal resistance.[58,59] Following the formation cycles, the Li/Mo_3S_{13} batteries demonstrated remarkable stability in their charge-discharge capacity, maintaining approximately 312 mAh g^{-1}

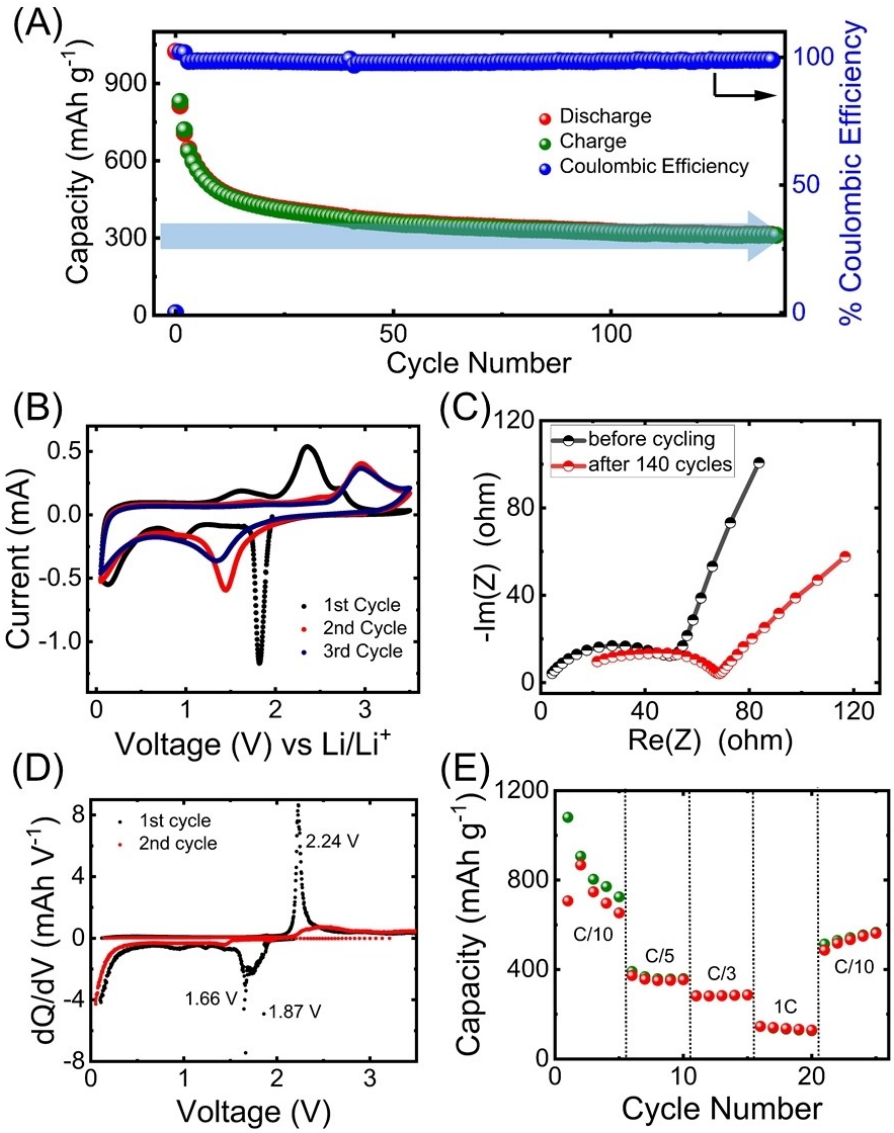

Figure 4. Capacity vs cycle number and Coulombic efficiency of the Li/Mo_3S_{13}, with blue arrow showing a sustained stability of the Li/Mo_3S_{13} cell (A). CV demonstrating the redox steps involved in the cycling processes; scan rate: 0.05 mV s^{-1} (B). EIS of Li/Mo_3S_{13} cell before cycling and after 140 cycles pointing at increase in cell resistance (C). The dQ/dV plot of Li/Mo_3S_{13} indicates the voltage plateaus at C/10 rate; resembling the CV result (D). Capacities of Li/Mo_3S_{13} cell at different current densities or C rates (red ball: discharge capacity, green ball: charge capacity), (E).

even after 140 cycles, with negligible capacity loss observed between successive cycles (Figure 4A). For instance, the capacity at the 50th cycle is 359 mAh g^{-1}, at the 100th cycle is 318 mAh g^{-1} and at the 140th cycle is 312 mAh g^{-1}, showing a loss of 11.4% percent from the 50th to the 100th and 1.9% from the 100th to the 140th cycle. This finding suggests an enhancement of the relative stability of Mo_3S_{13} electrodes with cycling. Coulombic efficiency (CE) of the charge-discharge processes remained very consistent throughout the cycling; around 100%, stating the reversibility of the charge-discharge properties of the material (Figure 4A). This finding suggests that Mo_3S_{13} exhibits remarkably higher specific capacity and cyclic stability compared to MoS_x chalcogel, the only other known chalcogel used as an electrode for LIBs (see Table 1). This could be attributed to the higher ratio of Mo to S in Mo_3S_{13} (Mo/S = 4.3) compared to MoS_x (Mo/S = 3.4), as well as the stability of the Mo_3S_{13} structure. However, the impact of the potential difference for the cycling of MoS_x (1–3.5 V) and Mo_3S_{13} chalcogel (0.05–3.5 V) cannot be completely ruled out. Moreover, a comparison with pure metal sulfides as high-performing electrode materials demonstrates that Mo_3S_{13} exhibits both high specific capacity and intriguing stability, as demonstrated in Table 1.

CV of the Li/Mo_3S_{13} half-cell shows distinguishable redox processes throughout the charge-discharge cycles (Figure 4B). In the first CV cycle, the redox peak appeared around 1.82 V representing the formation of nLi_2S and MoS_{y-n} ($Mo_3S_{13} \equiv MoS_y$).[60] The peak at 0.94 V is related to the intercalation of Li^+ into the gel matrix,[61,62] though it cannot be observed in the latter cycles, suggesting the irreversible nature

Table 1. Pure transition metal sulfides as sulfur-equivalent electrode materials in LIB applications.

Material	Voltage window [V]	Electrolyte	Current density or C rate	Cycle	Discharge cap. after [mAh g^{-1}]	Cycle trend	Refs.
Mo_3S_{13} chalcogel	0.05–3.50	1.2 M $LiPF_6$ in EC:EMC (3:7)	C/3 333 mA g^{-1}	140	312	Stable	This work
MoS_x chalcogel	1.00–3.50	1 M $LiPF_6$ in EC:EMC (3:7)	C/10	20	<300	Rapid decrease	[36]
MoS_2 (unexfoliated)	0.01–3.00	1 M $LiPF_6$ in EC:EMC (3:7)	50 mA g^{-1}	50	<200	Stable	[66]
MoS_3	1.00–3.00	1 M LiTFSI in PEGDME 500	50 mA g^{-1}	50	263	Getting stable	[67]
Amorphous $MoS_{5.7}$	1.50–3.00	1.2 M $LiPF_6$ in EC:DMC:FEC (1:1:0.26 v/v)	200 mA g^{-1}	300	355	Stable	[68]
MnS (rock-salt structure)	0.01–3.00	1 M LiBETI in EC:DEC:EMC (1:1:1)	100 mA g^{-1}	100 (600)	~150 (232.5)	Two-phase cycling	[69]
MnS (zinc blend structure)	0.01–3.00	1 M LiBETI in EC:DEC:EMC (1:1:1)	100 mA g^{-1}	100 (600)	~50 (287.9)	Two-phase cycling	[69]
MnS (wurtzite structure)	0.01–3.00	1 M LiBETI in EC:DEC:EMC (1:1:1)	100 mA g^{-1}	100 (600)	~10 (79.8)	Two-phase cycling	[69]
FeS_2	1.00–3.00	1 M $LiPF_6$ in EC:DMC (1:1)	C/2	100	234.2	Decrease	[32]
*Pyrite (FeS_2) nanocrystals	1.00–3.00	1 M $LiPF_6$ in EC:DMC + 3% FEC	200 mA g^{-1}	100	630	Stable	[65]
FeS microsphere	0.01–3.00	1 M $LiPF_6$ in EC:DEC (1:1)	100 mA g^{-1}	20	233	Getting stable	[70]
CoS_2	0.02–3.00	1 M $LiPF_6$ in EC:DMC (1:1)	200 mA g^{-1}	80	~200	Stable	[71]
TiS_2	1.50–2.80	1 M $LiPF_6$ in EC:DMC (1:1)	100 mA g^{-1}	120	~212	Very stable	[72]
VS_4 (prepared at 140 °C)	0.01–3.00	1 M $LiPF_6$ in EC:DEC (1:1)	C/20	100	~290	Getting stable	[73]
WS_2 (bulk. commercial)	0.01–3.00	1 M $LiPF_6$ in EC:DMC (1:1)	C/5	100	120	Getting stable	[74]
WS_2 (porous, synthesized)	0.01–3.00	1 M $LiPF_6$ in EC:DMC (1:1)	C/5	100	292.1	Getting stable	[74]

*synthesized using oleylamine as surfactant.

of the step. The main conversion/cathodic peak at 1.82 V in the 1st cycle shifts to 1.45 V in the 2nd cycle because of the breakdown of the polysulfide chains.[36] From the charge-discharge potential vs capacity plot (Figure S6A–B), it is evident that the material is applicable throughout a wide potential window. It is important to note that despite irreversibility in the initial cycling stage, the Li/Mo_3S_{13} cell gains stability over the cycling period; evinced from Figure S6B, which demonstrates that after 100 cycles the material doesn't show any significant fading. The attained stability could be due to the formation of MoS_2 nanoparticles as a minor secondary phase, resulting from a partial transformation of Mo_3S_{13} species; similar to MoS_3.[63] A comparison of EIS measurements between the freshly assembled cell and the cell after 140 cycles reveals a change in cell resistance (Figure 4C). An equivalent Randles circuit was built from the EIS data (Figure S6C) to calculate the cell resistance before and after cycling, the impedance data are given in Table S4. This increase in cell resistance with cycling primarily attributed to the formation of a resistive interfacial layer on the electrode surface, electrolyte decomposition resulting in reduced electrolyte conductivity, and the loss/dissolution of active materials.[37,64] The differential capacity plot, dQ/dV plot, of Li/Mo_3S_{13} cell shows the voltage plateaus at 1.87 and 1.66 V in the first discharge and at 2.24 V in the first charge at C/10 rate (Figure 4D). Each voltage plateau indicates a redox process, corroborating the findings observed in the CV analysis. It is discernible from Figures 4B and 4D that a significant change has happened to the electrode material in the first several cycles which justifies the capacity loss at the beginning of the charge-discharge process. In-situ and operando synchrotron X-ray and electron microscopic characterizations may unveil the origin of such capacity loss; however, this study is beyond the scope of this paper. The rate performance of Li/Mo_3S_{13} half-cell is displayed in Figure 4E. It indicates that the capacity loss occurred more rapidly in the initial cycles, similar to what was observed for cycling stability measurements (Figure 4A). It is worth mentioning that the Li/Mo_3S_{13} cell stabilizes after a few formation cycles at C/10 rate and subsequently shows stable capacity at C/5, C/3, and 1 C rates. Remarkably, after cycling at 1 C rate the cell revived to high capacity at C/10. The electrochemical performances of similar types of materials are displayed in Table 1. From Table 1 it is

convincing that the Mo_3S_{13} chalcogel is one of the best performing pure metal sulfides reported so far. The synthesis of this material was achieved without any additives, ligands or surfactants unlike the high-performing pyrites nanocrystals synthesized using oleylamine as surfactant, as shown in Table 1.[65]

3. Conclusions

Here we present the synthesis, characterization, and electrochemical properties of Mo_3S_{13}-based chalcogels. Detailed structural investigations of the local atomic arrangement of Mo_3S_{13}-based chalcogels by synchrotron X-ray PDF, XANES, and EXAFS, along with AIMD simulation, reveals a local structure similar to its molecular precursor $(NH_4)_2Mo_3S_{13}\cdot xH_2O$, however, each $Mo_3S_{13}{\equiv}Mo_3S(S_2)_6$ is connected randomly through S–S covalent bonding to form the matrix of Mo_3S_{13} chalcogel. Hence, the three-dimensional network of amorphous Mo_3S_{13} chalcogels embodies intrinsic properties, including nanoparticle-aggregated percolating porous features and a stable local structure. These properties, along with the semiconducting nature of Mo_3S_{13} gels, facilitate easy electron and Li-ion transfer across the electrode material, a characteristic may not be achievable with the crystalline molecular precursors of $(NH_4)_2Mo_3S_{13}\cdot xH_2O$. The Mo_3S_{13} gel exhibits good cyclic stability by maintaining capacity around 312 mAh g^{-1} at a C/3 rate even after 140 cycles. Despite an initial capacity loss, this material eventually attains stability, demonstrated by a loss of less than 2% capacity over the last 50 cycles. Mo_3S_{13} chalcogel exhibits superior electrochemical performances in terms of specific capacity, cycle-stability, and a wide potential window compared to reported metal-sulfides demonstrates promise for practical realization in LiSBs. Future studies should be dedicated to understanding the mechanisms responsible for capacity loss and gaining stability during different cycling stages.

Experimental Methods

Mo_3S_{13} Chalcogel Synthesis: $(NH_4)_2Mo_3S_{13}$ precursor was synthesized according to the method described previously.[47] To prepare the Mo_3S_{13} chalcogel, $(NH_4)_2Mo_3S_{13}$ (0.132 mmol) was dissolved in 3 mL of Formamide by ultrasound sonication for 90 minutes. Subsequently, a solution of I_2, obtained by dissolving I_2 (0.132 mmol) in 0.5 mL dimethylformamide, was added to the $(NH_4)_2Mo_3S_{13}$ solution and left for gelation at RT. The monolith wet gel with resilience against breaking from gentle shaking was formed in 48 hours. The aged wet gel was washed with 80% ethanol:water (4:1) mixture for 3 days and then with acetone for 3 days before drying at ambient conditions to produce the xerogel. Subsequently, the wet gels were washed with anhydrous ethanol to make aerogel at supercritical conditions (1200 psi and 35 °C) using liquid CO_2.

X-ray Powder Diffraction: High-resolution powder X-ray diffraction (PXRD) of the Mo_3S_{13} gel was collected from a Rigaku MiniFlex 600 diffractometer using Cu $K_{\alpha1}$ ($\lambda = 1.540593$ Å) radiation, generated from a sealed-tube X-ray source at 40 kV and 15 mA and the instrument was equipped with a D/teX Ultra detector. The diffraction intensity data were collected from 5 to 80° 2θ at a scan rate of 5° min^{-1} (0.02° resolution).

Raman Analysis: Macro Ram Raman Spectrometer with 785 nm integrated laser and adjustable power from 0–450 mW was used for the *operando* Raman spectroscopy of Mo_3S_{13} gel.

Electron Microscopy Imaging and Energy Dispersive Spectroscopy: The high-resolution SEM images were collected by using the Lyra3 – Tescan scanning electron microscopy (SEM) and was used for imaging and elemental analysis of the samples. The theoretical resolution of the instrument is 1.2 nm at 30 keV. An accelerating voltage of 20 kV and 120 s of accumulation time were maintained during data collection. Elemental analysis was performed using the ESED-II (environmental secondary electron detector). The powdered samples were placed on a carbon-taped metal stub for imaging of the surface morphology of the gels. Samples were verified by EDS and analysis of at least four different spots, with the average measured composition reported throughout. S/TEM analysis was performed using the Thermo Scientific™ Talos F200X scanning/transmission electron microscope at 200 kV acceleration voltage.

Solid-state UV/Vis optical diffuse reflectance spectroscopy: The solid-state UV/Vis spectra of the wet and xerogels were collected using a Shimadzu SolidSpec 3700 double beam, double monochromator spectrophotometer in the wavelength range of 200–2500 nm. $BaSO_4$ powder was used as a reference and base material on which the powder sample was coated. Using the Kubelka–Munk equation, the collected reflectance data were converted into absorbance: $\alpha/S = (1-R)^2/2R$, where R is the reflectivity, α is the absorption coefficient, and S is the scattering coefficient following the procedure described elsewhere.[75] The absorption edge was estimated by linearly extrapolating the absorption edge from the energy axis.

X-ray Photoelectron Spectroscopy: Finely ground powder of the chalcogels were placed on the conductive copper strips for the data collection: X-ray photoelectron spectroscopy (XPS) spectra of the as-obtained samples were collected using an ESCALAB 250Xi spectrometer (Thermo-Fisher) with Al–Kα X-ray as the radiation source, 500 μm spot size, and an electron flood gun to reduce sample charging. Before each spectra collection, the sample was etched with Ar at 30 KeV for 30 seconds. Each sample was measured in triplicate and all spectra have been corrected to the C1s peak at 284.8 eV.

Pair Distribution Function Analysis: Synchrotron total X-ray scattering data was collected from Advanced Photon Source (APS) of Argonne National Laboratory by the mail in ballot program using the 11-ID-B beamline at a wavelength of 0.1432 Å at ambient conditions. Prior to the experiment, the samples were ground to about the size of 50 μm and packed in the Kapton capillary. The rapid acquisition pair distribution function (RA-PDF) technique[76] was used to collect diffraction patterns at room temperature on powder samples. The data was integrated using the program Fit2D,[77] and corrections (subtraction of background and container) were performed using the program PDFgetX3.[78] The normalized data were truncated at 24 $Å^{-1}$ before PDF calculation. GSAS-II and PDFgui were used to analyze the data.[76,79]

For modeling efforts, the data was processed slightly differently. The data was integrated using pyFAI,[80] and reduced using PDFgetX3.[78] The data was truncated after 27.5 $Å^{-1}$. The diffpy-CMI program was used for modeling the data.[48] The single-cluster Mo_3S_{13} model was derived from the $(NH_4)_2Mo_3S_{13}$ structure,[81] and was isolated using the VESTA program.[82] The fittings were performed using the Debye equation with the several variables. First, a lattice parameter was defined in which the x, y, and z coordinates of each atom were multiplied by this variable to

simulate an expansion of the structure in lieu of unit cell parameters. Isotropic ADP parameters for Mo and S were assigned as well as the δ2 parameter which is related to the correlated atomic motion. A least-squares fitting built into the software was used to define R_w as the figure of merit.

Ab initio Molecular Dynamics (AIMD) Simulations: To model the structure of the Mo_3S_{13} chalcogel, amorphous (glasses) were generated through a melt-quench approach through AIMD simulations via the Vianna Ab initio Simulation Package (VASP).[83] The PBE exchange-correlation functional was used,[84] with the projected augmented wave (PAW) pseudopotentials for S and Mo, which included 3 $s^2 3p^4$ and 4$d^5$5 s^1 as the respective valence states. The plane-wave basis kinetic energy cutoff, E_{cutoff}, was set to 400 eV. Integration over the Brillouin zone (BZ) was accomplished with only Γ point considering the relatively large size of the simulation cell.

To create the melt-quenched system, we started with the $(NH_4)_2Mo_3S_{13}$ salt crystal structure, which contained two $(NH_4)_2Mo_3S_{13}$ units, and removed the ammonium (NH_4^+) groups from the structure. The internal coordinates for the two remaining (neutral) Mo_3S_{13} clusters were then relaxed. This unit cell was then used to construct a supercell of 3×3×3 containing 432 atoms (81 Mo atoms and 351 S atoms). The supercell was heated at 5000 K for 10 ps via an NVT-ensemble with a Nosé-Hoover thermostat. The temperature was then decreased to 2000 K for 10 ps. The system was then quenched at 300 K for 10 ps to generate the Mo_3S_{13} amorphous structure. A histogram (Figure S5) for the distribution of bonds versus pair correlation function (PCF) was created for the structure quenched at 300 K. The structure was then optimized via the DFT methods noted above to further evaluate the bond lengths.

X-ray Absorption Spectroscopy (XAS): XAS measurements were performed at the Very Sensitive Elemental and Structural Probe Employing Radiation from a Synchrotron (VESPERS, 07B2-1) beamline of the Canadian Light Source (CLS), Saskatoon, Canada. The VESPERS beamline is a hard X-ray microprobe beamline equipped with double crystal Si (111) and double multilayer monochromators. The double crystal Si (111) monochromator was used to scan the photon energy for Mo K-edge XANES and EXAFS measurements. The experiment was carried out using fluorescence mode, where the characteristic X-ray fluorescence from Mo was collected by a 4-element Vortex silicon drift detector and the incident flux by an N_2-filled ionization chamber. Powdered samples were sandwiched between Kapton tapes and were measured in ambient condition. The XANES and EXAFS analysis was done using python-based Larch,[85] and the FEFF calculations were done using FEFF 8 L with background correction by AUTOBK.[57] For the EXAFS fitting, the k-range was 2.00 to 12.00 $Å^{-1}$ and the R-range was 0.00 to 6.00 Å for the fitting in k-space and R-space respectively.

Electrochemical Analyses: Electrode slurry was prepared by mixing Mo_3S_{13} xerogel with conductive carbon (Super C65) and polyvinylidene fluoride (PVDF 5% in N-methylpyrrolidone, KUREHA 9300) binder with a mass ratio of 85:10:5 respectively, in N-methylpyrrolidone (NMP, Sigma-Aldrich) solvent. After mixing, the slurry was cast onto Cu foil and dried in a vacuum oven overnight. CR2032 coin cells were assembled in an Ar-filled glovebox (H_2O level $<$0.1 ppm, O_2 level $<$3 ppm) against Li metal. The mass loading of active material on the copper substrate was measured to be 0.85 mg. We have considered the total mass of Mo_3S_{13} chalcogel as active material mass. Celgard 2325 was used as the separator and 1.2 M $LiPF_6$ in ethylene carbonate (EC) and ethyl methyl carbonate (EMC) in a 3:7 weight ratio was used as the electrolyte. For cycling tests, half cells were cycled at C/3 rate between 0.05–3.50 V against Li/Li^+ using a Biologic MPG battery tester at 30 °C in a controlled environmental chamber (ESPEC). Electrochemical impedance spectroscopy (EIS) was performed for half-cells using the same Biologic MPG battery tester swept from 1 MHz to 1 Hz with a perturbation of 10 mV.

Supporting Information

EDS, dV/dD pore distribution curve, PDF fitting calculations, AIMD results, charge-discharge profile of Li/Mo_3S_{13} cell, equivalent Randles circuit from EIS data, and EXAFS fitting table of Mo_3S_{13} gel, impedance data of pristine and post-cycled cell.

Author Contributions

This manuscript was written through the contributions of all authors. All authors have given approval to the final version of the manuscript.

Acknowledgements

This work was supported by the US Department of Energy's Building EPSCoR-State/National Laboratory Partnerships DE-FOA-0002624. S. C. R. acknowledges the NSF Division of Chemistry (NSF-2100797). J. N., R. A. and O. O. are thankful to the US Department of Energy's Minority Serving Institution Partnership Program (MSIPP) managed by the Savannah River National Laboratory under SRNS contract (RFP No. 0000542525 and 0000458357). Electrochemical tests were performed at Oak Ridge National Laboratory, managed by UT-battelle, LLC for the US Department of Energy. This research used resources of the Advanced Photon Source; a U.S. Department of Energy (DOE) Office of Science User Facility operated for the DOE Office of Science by Argonne National Laboratory under Contract No. DE-AC02-06CH11357. The mail-in program at Beamline 11-ID–B (and/or 17-BM, 11-BM) contributed to the data. X-ray absorption spectroscopy measurements were performed at the VESPERS, Canadian Light Source, which is supported by the Canada Foundation for Innovation (CFI), the Natural Sciences and Engineering Research Council (NSERC), the National Research Council (NRC), the Canadian Institutes of Health Research (CIHR), the Government of Saskatchewan, and the University of Saskatchewan. Any use of trade, firm, or product names is for descriptive purposes only and does not imply endorsement by the U.S. Government. TEM and XPS were data were collected at the Chapel Hill Analytical and Nanofabrication Laboratory, CHANL, a member of the North Carolina Research Triangle Nanotechnology Network, RTNN, which is supported by the National Science Foundation, Grant ECCS-2025064, as part of the National Nanotechnology Coordinated Infrastructure, NNCI. A portion of this work was performed using XPS instrumentation supported by the Center for Hybrid Approaches in Solar Energy to Liquid Fuels (CHASE), an Energy Innovation Hub funded by the U.S. Department of Energy, Office of Science, Office of Basic Energy Sciences under Award Number DE-SC0021173. S. B., K. R. R., and C. R. acknowledge the University

of Kentucky (UK) Information Technology Department and Center for Computational Sciences (CCS) for providing supercomputing resources on the Lipscomb High Performance Computing Cluster.

Conflict of Interests

The authors declare no conflict of interest.

Data Availability Statement

Data is available upon request to the corresponding authors. ■■ Please carefully check the Data Availability Statement in your manuscript. Slightly different versions were detected upon export to production, we need you to confirm that the correct version appears. ■■

Keywords: Mo_3S_{13} chalcogels · aerogels · lithium-sulfide batteries · conversion-based batteries

[1] A. K. Stephan, *Joule* **2019**, *3*, 2583–2584.
[2] Y. Nishi, *J. Power Sources* **2001**, *100*, 101–106.
[3] J. Asenbauer, T. Eisenmann, M. Kuenzel, A. Kazzazi, Z. Chen, D. Bresser, *Sustain. Energy Fuels* **2020**, *4*, 5387–5416.
[4] A. Manthiram, *Nat. Commun.* **2020**, *11*, 1550.
[5] S. Urbonaite, T. Poux, P. Novák, *Adv. Energy Mater.* **2015**, *5*, 1500118.
[6] Y. V. Mikhaylik, J. R. Akridge, *J. Electrochem. Soc.* **2004**, *151*, A1969.
[7] R. Xu, J. Lu, K. Amine, *Adv. Energy Mater.* **2015**, *5*, 1500408.
[8] A. Manthiram, Y. Fu, S.-H. Chung, C. Zu, Y.-S. Su, *Chem. Rev.* **2014**, *114*, 11751–11787.
[9] H. Wang, Y. Yang, Y. Liang, J. T. Robinson, Y. Li, A. Jackson, Y. Cui, H. Dai, *Nano Lett.* **2011**, *11*, 2644–2647.
[10] W. Zhou, Y. Yu, H. Chen, F. J. DiSalvo, H. D. Abruña, *J. Am. Chem. Soc.* **2013**, *135*, 16736–16743.
[11] H. Al Salem, G. Babu, C. V. Rao, L. M. R. Arava, *J. Am. Chem. Soc.* **2015**, *137*, 11542–11545.
[12] X. Xu, W. Liu, Y. Kim, J. Cho, *Nano Today* **2014**, *9*, 604–630.
[13] J. Zhao, Y. Zhang, Y. Wang, H. Li, Y. Peng, *J. Energy Chem.* **2018**, *27*, 1536–1554.
[14] G. Whang, W. G. Zeier, *ACS Energy Lett.* **2023**, *8*, 5264–5274.
[15] R. Jin, Y. Jiang, G. Li, Y. Meng, *Electrochim. Acta* **2017**, *257*, 20–30.
[16] S. Wang, C. Qu, J. Wen, C. Wang, X. Ma, Y. Yang, G. Huang, H. Sun, S. Xu, *Mater. Chem. Front.* **2023**, *7*, 2779–2808.
[17] F. Jamal, A. Rafique, S. Moeen, J. Haider, W. Nabgan, A. Haider, M. Imran, G. Nazir, M. Alhassan, M. Ikram, Q. Khan, G. Ali, M. Khan, W. Ahmad, M. Maqbool, *ACS Appl. Nano Mater.* **2023**, *6*, 7077–7106.
[18] Y. Liu, Y. Qiao, W.-X. Zhang, Z. Li, X.-L. Hu, L.-X. Yuan, Y.-H. Huang, *J. Mater. Chem.* **2012**, *22*, 24026.
[19] D. T. Tran, S. S. Zhang, *J. Mater. Chem. A* **2015**, *3*, 12240–12246.
[20] A. Hua, W. Zhou, Y. Li, S. Li, R. Cheng, J. Yang, J. Luan, X. Wang, C. Jiang, D. Li, S. Ma, W. Liu, Z. Zhang, *J. Alloys Compd.* **2022**, *895*, 162668.
[21] S. Ni, X. Yang, T. Li, *J. Mater. Chem.* **2012**, *22*, 2395.
[22] W. Duan, W. Yan, X. Yan, H. Munakata, Y. Jin, K. Kanamura, *J. Power Sources* **2015**, *293*, 706–711.
[23] X. Li, S.-H. Qi, W.-C. Zhang, Y.-Z. Feng, J.-M. Ma, *Rare Met.* **2020**, *39*, 1239–1255.
[24] Q. Wang, L. Jiao, Y. Han, H. Du, W. Peng, Q. Huan, D. Song, Y. Si, Y. Wang, H. Yuan, *J. Phys. Chem. C* **2011**, *115*, 8300–8304.
[25] P. S. Murphin Kumar, V. Ponnusamy, H. Kim, M. A. Hernández-Landaverde, S. K. Krishnan, U. Pal, *ACS Appl. Energ. Mater.* **2022**, *5*, 6734–6745.
[26] Y.-Z. Wang, X.-Y. Shan, D.-W. Wang, Z.-H. Sun, H.-M. Cheng, F. Li, *Joule* **2018**, *2*, 1278–1286.
[27] Y. Xu, K. Wang, Z. Yao, J. Kang, D. Lam, D. Yang, W. Ai, C. Wolverton, M. C. Hersam, Y. Huang, W. Huang, V. P. Dravid, J. Wu, *Small* **2021**, *17*, 2100637.
[28] S. Kim, Y. J. Kim, W.-H. Ryu, *Appl. Surf. Sci.* **2021**, *547*, 149029.
[29] D. Wang, Y. Liu, X. Meng, Y. Wei, Y. Zhao, Q. Pang, G. Chen, *J. Mater. Chem. A* **2017**, *5*, 21370–21377.
[30] T. Matsuyama, A. Hayashi, T. Ozaki, S. Mori, M. Tatsumisago, *J. Mater. Chem. A* **2015**, *3*, 14142–14147.
[31] U. Chang, H. Lee, K. Eom, *ECS Meet. Abstr.* **2019**, *MA2019-02*, 283–283.
[32] J. Zou, J. Zhao, B. Wang, S. Chen, P. Chen, Q. Ran, L. Li, X. Wang, J. Yao, H. Li, J. Huang, X. Niu, L. Wang, *ACS Appl. Mater. Interfaces* **2020**, *12*, 44850–44857.
[33] C. Sun, K. Zhao, Y. He, J. Zheng, W. Xu, C. Zhang, X. Wang, M. Guo, L. Mai, C. Wang, M. Gu, *ACS Appl. Mater. Interfaces* **2019**, *11*, 20762–20769.
[34] M. Zhang, C. Tang, W. Cheng, L. Fu, *J. Alloys Compd.* **2021**, *855*, 157432.
[35] Z. Liu, H. Deng, P. P. Mukherjee, *ACS Appl. Mater. Interfaces* **2015**, *7*, 4000–4009.
[36] V. V. T. Doan-Nguyen, K. S. Subrahmanyam, M. M. Butala, J. A. Gerbec, S. M. Islam, K. N. Kanipe, C. E. Wilson, M. Balasubramanian, K. M. Wiaderek, O. J. Borkiewicz, K. W. Chapman, P. J. Chupas, M. Moskovits, B. S. Dunn, M. G. Kanatzidis, R. Seshadri, *Chem. Mater.* **2016**, *28*, 8357–8365.
[37] T. Islam, M. Li, A. Blanton, K. A. Pitton, K. R. Rao, S. Bayat, K. M. Wiaderek, M. A. Weret, S. C. Roy, R. Feng, D. Li, R. Alam, J. Nie, O. Oketola, A. Pramanik, B. S. Guiton, C. Risko, I. Belharouak, R. Amin, S. M. Islam, *ACS Energy Lett.* **2023**, 1–9. ■■Dear Author, if the journal has volumes, please add the journal number■■
[38] Z. W. Seh, J. H. Yu, W. Li, P.-C. Hsu, H. Wang, Y. Sun, H. Yao, Q. Zhang, Y. Cui, *Nat. Commun.* **2014**, *5*, 5017.
[39] K. Zhang, F. Chen, H. Pan, L. Wang, D. Wang, Y. Jiang, L. Wang, Y. Qian, *Inorg. Chem. Front.* **2019**, *6*, 477–481.
[40] F. Xi, F. Bozheyev, X. Han, M. Rusu, J. Rappich, F. F. Abdi, P. Bogdanoff, N. Kaltsoyannis, S. Fiechter, *ACS Appl. Mater. Interfaces* **2022**, *14*, 52815–52824.
[41] J. Kibsgaard, T. F. Jaramillo, F. Besenbacher, *Nat. Chem.* **2014**, *6*, 248–253.
[42] A. Blanton, T. Islam, S. C. Roy, A. Celik, J. Nie, D. R. Baker, D. Li, K. Taylor-Pashow, X. Zhu, A. Pramanik, R. Amin, R. Feng, R. Chernikov, S. M. Islam, *Chem. Mater.* **2023**, acs.chemmater.3c01675. ■■Dear Author, if the journal has volumes, please add the journal number■■
[43] J. L. Mohanan, I. U. Arachchige, S. L. Brock, *Science* **2005**, *307*, 397–400.
[44] S. Bag, P. N. Trikalitis, P. J. Chupas, G. S. Armatas, M. G. Kanatzidis, *Science* **2007**, *317*, 490–493.
[45] M. Thommes, K. Kaneko, A. V. Neimark, J. P. Olivier, F. Rodriguez-Reinoso, J. Rouquerol, K. S. W. Sing, *Pure Appl. Chem.* **2015**, *87*, 1051–1069.
[46] A. Müller, S. Sarkar, R. G. Bhattacharyya, S. Pohl, M. Dartmann, *Angew. Chem. Int. Ed. Engl.* **1978**, *17*, 535–535.
[47] S. M. Islam, J. D. Cain, F. Shi, Y. He, L. Peng, A. Banerjee, K. S. Subrahmanyam, Y. Li, S. Ma, V. P. Dravid, M. Grayson, M. G. Kanatzidis, *Chem. Mater.* **2018**, *30*, 3847–3853.
[48] P. Juhás, C. L. Farrow, X. Yang, K. R. Knox, S. J. L. Billinge, *Acta Crystallogr. Sect. Found. Adv.* **2015**, *71*, 562–568.
[49] A. Hjorth Larsen, J. Jørgen Mortensen, J. Blomqvist, I. E. Castelli, R. Christensen, M. Dułak, J. Friis, M. N. Groves, B. Hammer, C. Hargus, E. D. Hermes, P. C. Jennings, P. Bjerre Jensen, J. Kermode, J. R. Kitchin, E. Leonhard Kolsbjerg, J. Kubal, K. Kaasbjerg, S. Lysgaard, J. Bergmann Maronsson, T. Maxson, T. Olsen, L. Pastewka, A. Peterson, C. Rostgaard, J. Schiøtz, O. Schütt, M. Strange, K. S. Thygesen, T. Vegge, L. Vilhelmsen, M. Walter, Z. Zeng, K. W. Jacobsen, *J. Phys. Condens. Matter* **2017**, *29*, 273002.
[50] L. Yang, L. Xie, M. Chu, H. Wang, M. Yuan, Z. Yu, C. Wang, H. Yao, S. M. Islam, K. Shi, D. Yan, S. Ma, M. G. Kanatzidis, *Angew. Chem. Int. Ed.* **2022**, *61*, DOI 10.1002/anie.202112511.
[51] S. M. Islam, K. S. Subrahmanyam, C. D. Malliakas, M. G. Kanatzidis, *Chem. Mater.* **2014**, *26*, 5151–5160.
[52] S. M. Islam, C. D. Malliakas, D. Sarma, D. C. Maloney, C. C. Stoumpos, O. Y. Kontsevoi, A. J. Freeman, M. G. Kanatzidis, *Chem. Mater.* **2016**, *28*, 7332–7343.
[53] S. M. Islam, S. Vanishri, H. Li, C. C. Stoumpos, J. A. Peters, M. Sebastian, Z. Liu, S. Wang, A. S. Haynes, J. Im, A. J. Freeman, B. Wessels, M. G. Kanatzidis, *Chem. Mater.* **2015**, *27*, 370–378.
[54] S. M. Islam, V. K. Sangwan, Y. Li, J. Kang, X. Zhang, Y. He, J. Zhao, A. Murthy, S. Ma, V. P. Dravid, M. C. Hersam, M. G. Kanatzidis, *ACS Appl. Mater. Interfaces* **2018**, *10*, 38193–38200.

[55] S. M. Islam, J. Im, A. J. Freeman, M. G. Kanatzidis, *Inorg. Chem.* **2014**, *53*, 4698–4704.
[56] S. E. Shadle, J. E. Penner-Hahn, H. J. Schugar, B. Hedman, K. O. Hodgson, E. I. Solomon, *J. Am. Chem. Soc.* **1993**, *115*, 767–776.
[57] M. Newville, *J. Synchrotron Radiat.* **2001**, *8*, 96–100.
[58] J.-S. Kim, Y.-T. Park, *J. Power Sources* **2000**, *91*, 172–176.
[59] P. Arora, R. E. White, M. Doyle, *J. Electrochem. Soc.* **1998**, *145*, 3647–3667.
[60] J. Wang, S. H. Ng, S. Y. Chew, D. Wexler, G. X. Wang, H. K. Liu, *Electrochem. Solid-State Lett.* **2007**, *10*, A204.
[61] K. Chang, W. Chen, *ACS Nano* **2011**, *5*, 4720–4728.
[62] T. Wang, C. Sun, M. Yang, G. Zhao, S. Wang, F. Ma, L. Zhang, Y. Shao, Y. Wu, B. Huang, X. Hao, *J. Alloys Compd.* **2017**, *716*, 112–118.
[63] U. Chang, J. T. Lee, J.-M. Yun, B. Lee, S. W. Lee, H.-I. Joh, K. Eom, T. F. Fuller, *ACS Nano* **2018**, acsnano.8b07191. ■■Dear Author, if the journal has volumes, please add the journal number■■
[64] T. Osaka, S. Nakade, M. Rajamäki, T. Momma, *J. Power Sources* **2003**, *119–121*, 929–933.
[65] M. Walter, T. Zünd, M. V. Kovalenko, *Nanoscale* **2015**, *7*, 9158–9163.
[66] J. Xiao, D. Choi, L. Cosimbescu, P. Koech, J. Liu, J. P. Lemmon, *Chem. Mater.* **2010**, *22*, 4522–4524.
[67] J. Wang, S. H. Ng, S. Y. Chew, D. Wexler, G. X. Wang, H. K. Liu, *Electrochem. Solid-State Lett.* **2007**, *10*, A204.
[68] X. Wang, K. Du, C. Wang, L. Ma, B. Zhao, J. Yang, M. Li, X.-X. Zhang, M. Xue, J. Chen, *ACS Appl. Mater. Interfaces* **2017**, *9*, 38606–38611.
[69] Y. Hao, C. Chen, X. Yang, G. Xiao, B. Zou, J. Yang, C. Wang, *J. Power Sources* **2017**, *338*, 9–16.
[70] C. Xing, D. Zhang, K. Cao, S. Zhao, X. Wang, H. Qin, J. Liu, Y. Jiang, L. Meng, *J. Mater. Chem. A* **2015**, *3*, 8742–8749.
[71] J. M. Yan, H. Z. Huang, J. Zhang, Z. J. Liu, Y. Yang, *J. Power Sources* **2005**, *146*, 264–269.
[72] A. Chaturvedi, P. Hu, V. Aravindan, C. Kloc, S. Madhavi, *J. Mater. Chem. A* **2017**, *5*, 9177–9181.
[73] X. Chen, Y. Lu, C. Feng, *J. Mater. Sci. Mater. Electron.* **2019**, *30*, 9695–9704.
[74] M. Z. Ansari, S. A. Ansari, N. Parveen, M. H. Cho, T. Song, *New J. Chem.* **2018**, *42*, 5859–5867.
[75] R. Roccanova, W. Ming, V. R. Whiteside, M. A. McGuire, I. R. Sellers, M.-H. Du, B. Saparov, *Inorg. Chem.* **2017**, *56*, 13878–13888.
[76] P. J. Chupas, X. Qiu, J. C. Hanson, P. L. Lee, C. P. Grey, S. J. L. Billinge, *J. Appl. Crystallogr.* **2003**, *36*, 1342–1347.
[77] A. P. Hammersley, S. O. Svensson, M. Hanfland, A. N. Fitch, D. Hausermann, *High Pressure Res.* **1996**, *14*, 235–248.
[78] P. Juhás, T. Davis, C. L. Farrow, S. J. L. Billinge, *J. Appl. Crystallogr.* **2013**, *46*, 560–566.
[79] B. H. Toby, R. B. Von Dreele, *J. Appl. Crystallogr.* **2013**, *46*, 544–549.
[80] J. Kieffer, V. Valls, N. Blanc, C. Hennig, *J. Synchrotron Radiat.* **2020**, *27*, 558–566.
[81] A. Müller, S. Sarkar, R. G. Bhattacharyya, S. Pohl, M. Dartmann, *Angew. Chem. Int. Ed. Engl.* **1978**, *17*, 535–535.
[82] K. Momma, F. Izumi, *J. Appl. Crystallogr.* **2011**, *44*, 1272–1276.
[83] G. Kresse, J. Hafner, *Phys. Rev. B* **1993**, *47*, 558–561.
[84] J. P. Perdew, K. Burke, M. Ernzerhof, *Phys. Rev. Lett.* **1996**, *77*, 3865–3868.
[85] M. Newville, *Astrophys. Source Code Libr.* **2017**, ascl:1703.001. ■■Dear Author, if the journal has volumes, please add the journal number■■

Manuscript received: February 25, 2024
Revised manuscript received: March 15, 2024
Accepted manuscript online: March 22, 2024
Version of record online: ■■, ■■

RESEARCH ARTICLE

This study showcases the synthesis and analysis of the local structure of amorphous Mo_3S_{13} within chalcogel matrix and underscores its potential as high-capacity electrode for Li-ion battery applications.

T. Islam, S. Chandra Roy, S. Bayat, M. Adigo Weret, J. M. Hoffman, K. R. Rao, C. Sawicki, J. Nie, R. Alam, O. Oketola, C. L. Donley, A. Kumbhar, R. Feng, K. M. Wiaderek, C. Risko, R. Amin, S. M. Islam**

1 – 13

Mo_3S_{13} Chalcogel: A High-Capacity Electrode for Conversion-Based Li-Ion Batteries

ORCID (Open Researcher and Contributor ID)

Please check that the ORCID identifiers listed below are correct. We encourage all authors to provide an ORCID identifier for each coauthor. ORCID is a registry that provides researchers with a unique digital identifier. Some funding agencies recommend or even require the inclusion of ORCID IDs in all published articles, and authors should consult their funding agency guidelines for details. Registration is easy and free; for further information, see http://orcid.org/.

Carrie L. Donley
Misganaw Adigo Weret
Ruhul Amin http://orcid.org/0000-0002-0054-3510
Keerthan R. Rao
Subrata Chandra Roy
Chad Risko
Conrad Sawicki
Renfei Feng
Taohedul Islam
Sahar Bayat
Amar Kumbhar
Robiul Alam
Jing Nie
Oluwaseun Oketola
Saiful M. Islam http://orcid.org/0000-0001-8518-1856
Justin M. Hoffman
Kamila M. Wiaderek

Author Contributions

Taohedul Islam: Data curation:Lead; Formal analysis:Lead; Software:Lead; Visualization:Lead; Writ-

ing – original draft:Lead; Writing – review & editing:Lead
Subrata Chandra Roy: Data curation:Supporting; Formal analysis:Equal; Writing – review & editing:Supporting
Sahar Bayat: Formal analysis:Equal; Software:Lead; Writing – review & editing:Supporting
Misganaw Adigo Weret: Formal analysis:Equal; Writing – review & editing:Supporting
Justin M. Hoffman: Formal analysis:Equal; Software:Lead; Writing – review & editing:Supporting
Keerthan R Rao: Software:Supporting
Conrad Sawicki: Formal analysis:Equal
Jing Nie: Formal analysis:Supporting
Robiul Alam: Formal analysis:Supporting
Oluwaseun Oketola: Formal analysis:Supporting
Carrie L. Donley: Formal analysis:Equal
Amar Kumbhar: Formal analysis:Equal
Renfei Feng: Formal analysis:Equal
Kamila M. Wiaderek: Formal analysis:Supporting
Chad Risko: Conceptualization:Equal; Methodology:Equal; Supervision:Supporting; Writing – review & editing: Supporting
Ruhul Amin: Conceptualization:Equal; Formal analysis:Supporting; Supervision:Supporting; Writing – review & editing:Supporting
Saiful M. Islam: Conceptualization:Lead; Funding acquisition:Lead; Methodology:Lead; Project administration:Lead; Resources:Lead; Supervision:Lead; Writing – review & editing:Lead